Check for updates

Improved ORR/OER bifunctional catalytic performance of amorphous manganese oxides prepared by photochemical metal–organic deposition†

Fan Bai, [iD] ‡[a] Yuxiu He,‡[b] Lincheng Xu,[ac] Yue Wang,[a] Yan Wang,[a] Zhanzhong Hao*[c] and Fan Li [iD] *[a]

Transition metal oxide nanomaterials or nanocomposites containing transition metal oxides have the potential to replace traditional catalysts for electrochemical applications, photocatalysis, and energy storage. Amorphous manganese oxide catalysts were prepared *via* photochemical metal–organic deposition (PMOD). Through XRD, SEM-EDS, Raman spectroscopy, FTIR spectroscopy, HRTEM-EDS, and XPS, we confirmed that amorphous manganese oxide catalysts were successfully prepared. Amorphous catalysts prepared with different photolysis times were compared in terms of their performance for the oxygen reduction reaction (ORR) and oxygen evolution reaction (OER), and catalyst MnO_x-PMOD48 showed the best performance because of its high Mn^{3+} proportion and electrochemically active surface area. MnO_x-PMOD48 showed better ORR/OER performance than the crystalline MnO_x and MnO_x/Ti_4O_7 catalysts from our previous work. Following our previous work on crystalline manganese oxide catalysts, we added Ti_4O_7 during the PMOD process with 48 h of treatment and obtained the amorphous catalyst MnO_x/Ti_4O_7-PMOD. MnO_x/Ti_4O_7-PMOD was supported by Ti_4O_7 particles, which led to improved stability. The ORR/OER catalytic activity of MnO_x/Ti_4O_7-PMOD was better than that of crystalline catalyst MnO_x/Ti_4O_7-300, which was the best crystalline catalyst in our previous work. We also compared lithium-oxygen batteries assembled with MnO_x/Ti_4O_7-PMOD and MnO_x/Ti_4O_7-300. The battery performance tests confirmed that the amorphous manganese catalyst had better ORR/OER bifunctional catalytic performance than the crystalline manganese catalyst because of its high defect state with more abundant edge active sites and more surface-exposed catalytic active sites.

1. Introduction

New material technologies play a key role in clean energy and low-carbon technologies. Thermoelectric materials, including organic, inorganic, and hybrid organic–inorganic materials, are widely considered suitable materials for thermoelectric devices.[1] Nanostructured metal oxides and their hybrids have attracted significant attention from researchers for photocatalytic, anticancer, and antibacterial applications.[2,3] Nanocomposite membranes are at the heart of the process for pervaporation separation techniques.[4,5] Carbon neutrality is the new mission for future generations and the planet as a whole. It

is increasingly clear that reducing the use of fossil energy, turning to green energy, and emphasising low-carbon lifestyles and production techniques must be the new direction for mankind. Metal–air batteries are clean, low-carbon, safe, and efficient new energy systems with the advantages of high energy density and large output power.[6] However, owing to factors like poor cyclic stability, large differences in charge–discharge voltage, and slow reaction kinetics, further application of metal–air batteries is greatly restricted. Many studies have shown that the slow reaction kinetics of the oxygen reduction reaction (ORR) and oxygen evolution reaction (OER) at the air electrode limit the performance improvement of metal–air batteries.[7–9] Therefore, it is urgent to develop efficient and stable ORR/OER bifunctional catalysts to promote the development of metal–air batteries.

Noble metals, such as platinum and iridium, are highly efficient and widely used ORR/OER catalysts.[10–13] But the scarcity and high cost of noble metals are the main reasons that restrict their further widespread use, especially for replacing traditional energy sources with clean energy sources in every

[a]*Faculty of Environment and Life Sciences, Beijing University of Technology, Beijing, 100124, P. R. China. E-mail: vanadiumli@bjut.edu.cn*

[b]*Beijing Office of Metrohm China Ltd, Beijing 100085, P. R. China*

[c]*College of Chemistry, Baotou Teachers College, Bao Tou 014030, P. R. China. E-mail: 18438602389@163.com*

† Electronic supplementary information (ESI) available. See DOI: 10.1039/d1ra08618a

‡ These authors contributed equally to this work.

aspect of our lives.[14] Mixed metal oxide nanocomposites (rare-earth-based) are a target for antibacterial, electrochemical, and photocatalytic research.[15] Transition metals with large storage, low cost, and relatively high catalytic performance are very suitable substitutes for noble metals.[16] Co/Ni metal nanostructures have been reported as efficient photocatalysts.[17] Transition metal sulfides used in supercapacitors have also attracted broad attention.[18] Among these transition metals, manganese is of particular interest because of its varied valencies and its ability to form a variety of oxides.[19–21] Most of them, such as MnO_2, Mn_2O_3, and Mn_3O_4, have been confirmed to be efficient ORR/OER catalysts.[22] In particular, Mn^{3+} has been found to be the key to ORR/OER bifunctional catalysis.[23–25] Manganese oxides have also been used in the Fischer–Tropsch (FT) process to improve the selectivity of long-chain carbon products.[26] Manganese oxide remains stable over a wide pH range at a certain potential. Therefore, manganese oxide is a potentially efficient and stable catalyst.

In our previous work, we prepared crystalline manganese oxide to test its catalytic performance.[27] Catalysts used in practical applications all contain defects. Srinivas showed that a smaller crystal size leads to the occurrence of oxygen vacancies at the surface and grain boundaries, which enhances catalytic performance.[17] For transition metal oxides, the increase in surface defects can provide more active sites to improve catalytic activity and ameliorate the problem of poor conductivity.[28,29] It is worth studying how to control the increase in defects during the preparation process to improve the catalytic activity. The synthesis of amorphous catalytic materials, or materials with high defects, can help to provide more active sites in another way. Several physical and chemical methods have been reported for preparing 2-dimensional (2D) film nanomaterials.[30] Photochemical metal–organic deposition (PMOD) has been used to successfully prepare manganese oxide amorphous materials.[31,32] The PMOD strategy has also been used in the synthesis of amorphous oxides of lead, iron, cobalt, and nickel, and related studies have confirmed that the catalytic performance of amorphous catalysts is superior to that of the corresponding crystalline materials.[33–37] Although the conductivity of metal oxide nanomaterials or amorphous materials can be improved by changing their bandgap energy, it is still not as good as that of metallic or carbon materials. To improve the electrical conductivity, metal oxide nanomaterials or amorphous materials can be combined with other conductive carriers. In energy storage supercapacitors and solar cells, polyaniline combines with graphene and improves the conductivity by working as an organic conductive polymer.[38] Apart from improving the conductivity, SiO_2 carriers have been used to improve the surface area of the nanomaterial.[39]

In this study, we synthesised amorphous manganese oxide catalysts using the PMOD method and introduced carbon particles to improve the electrical conductivity. Different catalysts were synthesized by controlling the irradiation time, and their phases and catalytic activities were compared to explore the essential relationship between the synthesis strategy and catalytic activity. The optimum amorphous catalyst was compared with the crystalline catalysts prepared in our previous

work. The disappearance of defects from amorphous catalytic materials is an important cause of catalyst deactivation. To address this issue, we referred to our experience in the preparation of crystalline catalysts and introduced Ti_4O_7 as a support material. We then compare the resulting catalyst with the optimal crystalline catalyst supported by Ti_4O_7 from our previous work. Finally, we concluded that amorphous MnO_x/Ti_4O_7-PMOD is the best catalyst for our system.

2. Experimental

2.1 Sample synthesis

Amorphous manganese oxides were synthesised *via* PMOD. Manganese(II) 2-ethylhexanoate (7.1114 g, 6% manganese, Alfa Aesar), carbon powder XC-72 (0.3000 g, >99%, Alfa Aesar), and (A) none or (B) 0.3790 g Ti_4O_7 (>95%, Titanium Energy Technology) were dispersed in 5 mL *n*-hexane (>97%, TongGuang Fine Chemicals) in a watch glass and treated with an ultrasonic cleaner for 10 min. Three watch glasses of A were placed in a dark chamber with 254 and 185 nm ultraviolet (UV) light sources and one glass each was irradiated for 24, 48, and 72 h. One watch glass of B was placed in the same chamber and irradiated for 48 h. After UV irradiation, all the watch glasses were dried in a drying oven at 60 °C for 2 h. Amorphous manganese oxide MnO_x-PMOD samples prepared with different UV treatment durations were named MnO_x-PMOD24, MnO_x-PMOD48, and MnO_x-PMOD72. The amorphous MnO_x composited with Ti_4O_7 was named MnO_x/Ti_4O_7-PMOD. More details are provided in the ESI.†

2.2 Characterization methods

Phase analysis of the MnO_x-PMOD samples was performed using X-ray diffraction (XRD, Bruker D8 advance) at a scan rate of 10° min^{-1} from 10° to 80°. The morphology and microstructure were characterised using scanning electron microscopy (SEM, JEOL JSM-7900) and high-resolution transmission electron microscopy (HRTEM, FEI Tecnica G2 F20). Valence state analysis of the surface was carried out by X-ray photoelectron spectroscopy (XPS, ESCALAB 250Xi) with an Al Kα radiation source. To confirm the consumption of the manganese source, Fourier transform infrared (FTIR) spectroscopy was performed using a Bruker Vertex 70 spectrometer. Raman spectroscopy was performed using a Renishaw inVia™ Qontor instrument to confirm the formation of manganese oxides.

2.3 Electrochemical measurements

A three-electrode system was used in this study. A 5 mm-diameter glassy carbon (GC) controlled by a rotating ring and disk electrode (RRDE, IPS) was used as the working electrode, with a Hg/HgO reference electrode and carbon rod counter electrode. Cyclic voltammetry (CV), linear sweep voltammetry (LSV), and electrochemical impedance spectroscopy (EIS) were performed to evaluate the electrocatalytic performance. The electrode material was prepared by dispersing 2.0 mg MnO_x-PMOD sample in 1 mL anhydrous ethanol and 0.5 mL 0.2% Nafion ethanol solution and then forming a slurry using an

ultrasonic dispersing instrument. The electrode material slurry (20 μL) was added dropwise onto the GC working electrode using a microsyringe. The three-electrode system was installed in a customised electrolytic cell and submerged in 0.1 mol L^{-1} KOH solution saturated with argon for activation and then saturated with oxygen for electrochemical measurement. For chronoamperometry (CA) and polarisation curve tests, a GC piece (10 × 10 mm) was used as the working electrode. The above-mentioned formulation was used for the electrode material slurry; however, the slurry amount was changed to 200 μL, and all electrochemical tests were performed using a Metrohm Autolab PGSTAT302N electrochemical workstation without *iR* compensation.

2.4 Li–O$_2$ battery tests

The MnO$_x$-PMOD sample, conductive carbon black (Super P, >99%, Alfa Aesar), and an agglomerant (polyvinylidene fluoride, PVDF) were mixed in a mortar at a mass ratio of 3 : 6 : 1. Subsequently, *N*-methyl-2-pyrrolidinone (>99%, Aladdin) was added to configure the slurry. Carbon paper was used as the current collector substrate to spray the slurry. The whole electrode material was dried at 120 °C for 12 h in an oven and then cut into pieces 14 mm in diameter for assembling the battery. Finally, a CR2032 coin lithium–oxygen battery was assembled in an argon-filled glove box (Braun, Lab Star) and tested in a customised pure oxygen-filled battery box for charge and discharge tests (Neware, CT-4008). More details regarding the carbon paper electrode are provided in the ESI.†

3. Results and discussion

3.1 Phase identification and morphology analysis

The blue, red, and black curves in Fig. 1A show the XRD patterns of the amorphous manganese oxide MnO$_x$-PMOD samples obtained with different UV light decomposition times. Protrusions were observed around $2\theta = 28.9°$, and no peaks were found in

any of the three patterns. The samples prepared by PMOD did not show crystallisation and were still high-defect-state amorphous or primary crystallisation materials. From Fig. S1,† the absorption peaks at 2961 cm^{-1}, 2876 cm^{-1}, 2937 cm^{-1}, and 2853 cm^{-1} can be assigned to manganese(II) 2-ethylhexanoate from the organic manganese source used herein.[35,36] With increasing UV photolysis time, the intensities of the organic manganese absorption peaks decreased, indicating that the organic manganese source was consumed. We found a peak at approximately 650 cm^{-1} in all three Raman spectra, as shown in Fig. S2.† Compared with the standard Raman spectrogram, this peak corresponds to the Mn–O bond, and the peak intensity increases with increasing UV photolysis time. The FTIR and Raman results together show that the organic manganese source was converted to amorphous manganese oxides.

The SEM images in Fig. S3† show the microstructures of MnO$_x$-PMOD24, MnO$_x$-PMOD48, and MnO$_x$-PMOD72. The amorphous catalysts prepared by PMOD showed an irregular 2D morphology different from the 1D structure of crystalline manganese oxide. These surfaces had different degrees of folds and cracks. With different photolysis times, the morphologies of the catalysts showed similar film structures. For example, the energy dispersive spectrum (EDS) of MnO$_x$-PMOD72 (Fig. S4†) shows that manganese and oxygen mainly existed in the irregular 2D lamellar morphology, while carbon mainly existed in the form of XC-72 carbon particles in the substrate. The irregular 2D structure has the advantages of mechanical peeling control, large surface area, and abundant edge active sites, which will improve the catalyst performance.[40–43]

In the electrochemical tests, the catalysts were modified on the surface of the GC electrode to affect the real morphology. We dispersed MnO$_x$-PMOD48 in a Nafion–ethanol solution and performed SEM and EDS tests after natural drying. A SEM test was performed on an XC-72 sample subjected to the same treatment for comparison. The SEM images of MnO$_x$-PMOD48 and XC-72 show that the carbon nanoparticles were stacked in
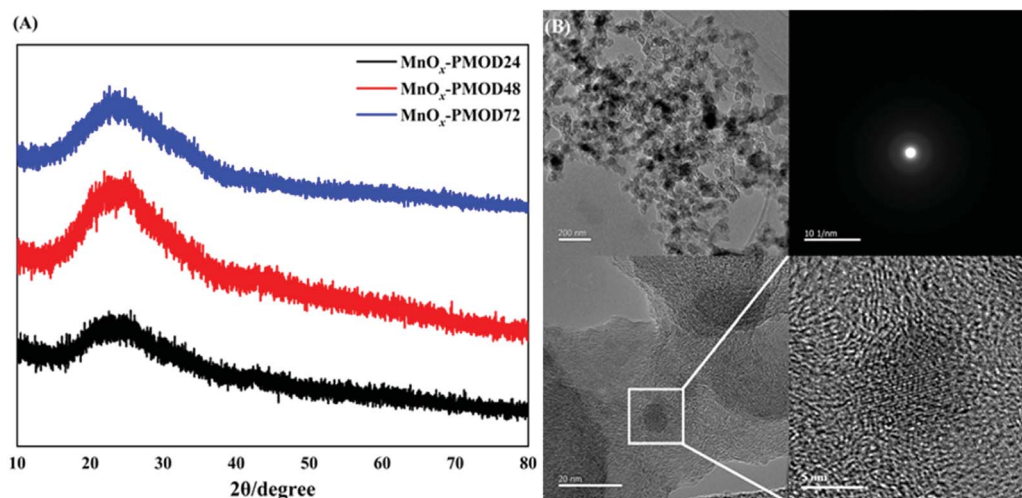

Fig. 1 (A) XRD patterns of MnO$_x$-PMOD24 (black), MnO$_x$-PMOD48 (red), MnO$_x$-PMOD72 (blue). (B) TEM and HRTEM images of MnO$_x$-PMOD48 after ultrasonic dispersion.

the same way, as shown in Fig. S5.† The MnO$_x$-PMOD48 nanoparticles appeared closer than those of XC-72. In other words, amorphous manganese oxide had no obvious shape characteristics after being dispersed in ethanol, and the original 2D structure disappeared. The EDS image of MnO$_x$-PMOD48 in Fig. S6† shows that manganese and oxygen were enriched in the carbon particles. In actual electrode materials, manganese oxides can be combined with XC-72 carbon particles. XC-72 can provide support for manganese oxides, which is helpful for improving the stability of catalysts during the catalytic process and reducing the crystallisation of manganese oxides. Amorphous manganese oxides were evenly dispersed in XC-72, which contributed to its better catalytic activity.

TEM characterisation was used to further explore the microstructure and the relationship between the amorphous manganese oxides and XC-72 carbon particles, as shown in Fig. 1B. In the TEM images, the morphology of crystalline manganese oxides was not observed, and only the accumulation of particles was observed. As shown in the HRTEM images in Fig. 1B, fuzzy lattice fringes appear within a narrow range of less than 10 nm, but it is difficult to match the crystal planes of crystalline manganese oxides. We believe that this nanoregion was formed by the initial crystallisation of manganese oxides. Amorphous manganese oxides began to show an ordered arrangement, but because of their high defect density, a stable and visible lattice structure could not be formed. In addition, the corresponding selective area electron diffraction image shows an obvious diffuse halo, and no regular spot group or diffraction ring is observed, which proves that the region existed in an amorphous form. The above characterisations confirm that catalysts composed of amorphous manganese oxide were successfully prepared.

3.2 Electrochemical properties and analysis

The ORR and OER performances of the amorphous catalysts MnO$_x$-PMOD24, MnO$_x$-PMOD48, and MnO$_x$-PMOD72 were compared using CV and LSV measurements, as shown in Fig. S7 and S8.† MnO$_x$-PMOD24 showed the worst catalytic activity for the ORR, as confirmed by the CV and ORR results. The ORR onset potentials of MnO$_x$-PMOD48 and MnO$_x$-PMOD72 were similar, and the ORR-limiting diffusion current of MnO$_x$-PMOD72 was the highest among the three catalysts. For the OER performance, MnO$_x$-PMOD48 showed the lowest overpotential at 10 mA cm^{-2} and the highest current density in the measurement potential range. MnO$_x$-PMOD48 showed better catalytic activity for the OER than MnO$_x$-PMOD24 and MnO$_x$-PMOD72. MnO$_x$-PMOD48 was found to be the best ORR/OER catalyst among the three tested catalysts. The electrochemical active surface area of each catalyst was estimated from the electrochemical double-layer capacitance (C_{DL}) of the catalytic surface and the specific capacitance, as shown in Fig. S9.† The C_{DL} was calculated from the CV measurements at different scan rates, and the scan range was ±60 mV around the open circuit potential of each catalyst. The C_{DL} calculation result for MnO$_x$-48 was 6.135 mF, compared with 2.785 and 4.355 mF for MnO$_x$-PMOD24 and MnO$_x$-PMOD72, respectively. MnO$_x$-PMOD48 had

a larger electrochemically active surface area than the other catalysts, leading to better catalytic performance. Therefore, we chose MnO$_x$-PMOD48 as the amorphous catalyst for subsequent tests.

According to Zhu *et al.*, using manganese(II) 2-ethyl-hexanoate as the raw material for UV photolysis should produce a mixture of MnO and Mn$_2$O$_3$.[32] The Mn^{2+} in MnO is unstable at room temperature and can continue to oxidise to MnO$_2$. Therefore, Mn^{2+}, Mn^{3+}, and Mn^{4+} may coexist on the surfaces of the as-prepared amorphous MnO$_x$ samples. Because all the generated products exist in amorphous form, the molecular formula shown in this work is convenient for characterising the valence state of manganese and the number of Mn–O bonds. The obtained valence state is not consistent with the actual form of manganese oxides.

XPS was used to determine the valence state of the MnO$_x$-PMOD24, MnO$_x$-PMOD48, and MnO$_x$-PMOD72 sample surfaces. The narrow sweep of manganese was limited to a binding energy of 632–660 eV, as shown in Fig. S10.† The Mn 2p spectrum includes two main regions, which can be divided into two peaks of Mn 2p$_{1/2}$ and Mn 2p$_{3/2}$. Based on the NIST XPS database and the previous XRD patterns, the valence states of the MnO$_x$-PMOD samples are identified as Mn^{2+}(2p$_{3/2}$ for 641.1 eV and 2p$_{1/2}$ for 653.0 eV), Mn^{3+}(2p$_{3/2}$ for 641.6 eV and 2p$_{1/2}$ for 653.3 eV), Mn^{4+}(2p$_{3/2}$ for 642.2 eV and 2p$_{1/2}$ for 653.8 eV). The peak areas and ratios of the samples at different calcination temperatures are listed in Table S1† for comparing the areas of Mn^{2+}, Mn^{3+}, and Mn^{4+}.

The Mn^{2+} ratio in the three catalysts was the highest at 24 h and decreased continuously on increasing the photolysis time to 72 h. In contrast, the Mn^{4+} ratio increased gradually. This result is consistent with the mechanism by which Mn^{2+} is oxidised to Mn^{4+} at room temperature. The Mn^{3+} ratio is unique in that the highest ratio was observed for MnO$_x$-PMOD24, *i.e.* after 24 h of UV photolysis. These results, in combination with the FTIR results in Fig. S1,† confirm that the oxidation of amorphous metal continued because of incomplete photolysis of the manganese source, and the ratio of Mn^{3+} increased slightly from MnO$_x$-PMOD24 to MnO$_x$-PMOD48. Because the manganese source had completely reacted from MnO$_x$-PMOD48 to MnO$_x$-PMOD72, the formation of Mn^{3+} is ended. Because of the high stability of Mn^{3+}, only a small amount of Mn^{3+} was further oxidised to Mn^{4+}; thus, the Mn^{3+} ratio was only slightly reduced. In our previous work, we found that the Mn^{3+} ratio obviously impacted the catalytic performance.[27] The electrochemical tests have proved that MnO$_x$-PMOD48 is the best catalyst among the three tested herein.

The ORR and OER performances of the amorphous catalyst MnO$_x$-PMOD48 and crystalline catalysts MnO$_x$ and MnO$_x$/Ti$_4$O$_7$ were evaluated by LSV measurements, as shown in Fig. 2A. MnO$_x$ and MnO$_x$/Ti$_4$O$_7$ are crystalline manganese oxide catalysts obtained in a previous work. The MnO$_x$/Ti$_4$O$_7$ catalyst includes Ti$_4$O$_7$ as a catalyst support. The ORR onset potential of MnO$_x$-PMOD48 was higher than those of MnO$_x$ and MnO$_x$/Ti$_4$O$_7$, and the ORR-limiting diffusion current density of MnO$_x$-PMOD48 was the highest. In terms of OER performance, MnO$_x$-PMOD48 showed the lowest overpotential at 10 mA cm^{-2} for the
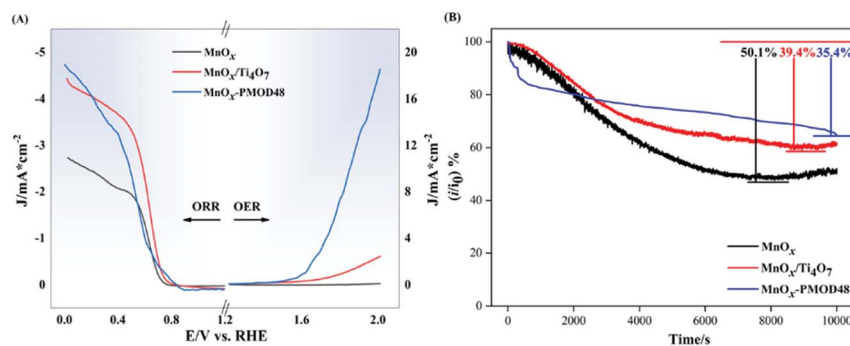
Fig. 2 (A) OER/ORR performance of amorphous catalyst MnO_x-PMOD48 and crystalline catalysts MnO_x and MnO_x/Ti_4O_7 at a rate of 10 mV s^{-1} after saturated with O_2. (B) Chronoamperometry tests of MnO_x-PMOD48, MnO_x, and MnO_x/Ti_4O_7.

OER and the highest current in the measurement potential range, whereas the OER currents of MnO_x and MnO_x/Ti_4O_7 did not reach 10 mA cm^{-2}. This result is consistent with the fact that amorphous manganese oxides exhibit better ORR/OER performance than crystalline manganese oxides. Chronoamperometry tests were performed to compare the stability of the catalysts, as shown in Fig. 2B. After a 10 000 s test at 0.68 V *vs.* RHE, the current of MnO_x-PMOD48 decreased by 35.4% compared with the initial current. The current declined by 50.1% and 39.4% for MnO_x and MnO_x/Ti_4O_7, respectively. Therefore, amorphous manganese oxide showed improved stability, performing even better than the Ti_4O_7-supported crystalline catalyst MnO_x/Ti_4O_7.

3.3 Influence of Ti_4O_7 on manganese oxides

In our previous work, adding Ti_4O_7 particles into a crystalline catalyst led to better performance.[27] This is mainly because Ti_4O_7 induces the growth of manganese oxides and increases the number of active sites. The Ti_4O_7 particles also had a supporting effect on the MnO_x catalyst. We tested the effect of Ti_4O_7 on the amorphous manganese oxides. The XRD, SEM, TEM, and EDS mapping results in Fig. 3 show the microstructure and elemental distribution of the amorphous catalyst MnO_x/Ti_4O_7-PMOD. In Fig. 3A, the peaks at $2\theta = 26.38°$ and $31.76°$ can be assigned to Ti_4O_7 (PDF#71-1428) and no peaks corresponding to the crystal planes of manganese oxide were observed. The introduction of Ti_4O_7 did not affect the formation of amorphous manganese oxides. The distribution of titanium was different from those of manganese and oxygen in the SEM image, as shown in Fig. 3B. The manganese oxides showed 2D growth on the Ti_4O_7 particles. Therefore, the surface of MnO_x/Ti_4O_7-PMOD is more concave and convex than that of MnO_x-PMOD48, which leads to more folds and introduces more marginal active sites. This result is consistent with that of our previous work. In Fig. 3C, the TEM image of MnO_x/Ti_4O_7-PMOD shows that the Ti_4O_7 particle size was approximately 100 nm, and no lattice characteristics of manganese oxide were observed. According to the EDS mapping results in Fig. 3C, the distribution of titanium, manganese, and oxygen was identical, which confirms the above speculation about the growth of amorphous manganese oxide on Ti_4O_7 particles. Amorphous manganese oxides

have low stability and are easy to crystallise. Because of the support and stabilisation of Ti_4O_7 particles, amorphous manganese oxide can be maintained well, which may further improve the catalytic performance and stability of MnO_x/Ti_4O_7-PMOD.

We chose MnO_x/Ti_4O_7-PMOD as the best amorphous manganese oxide catalyst to compare with crystalline catalyst MnO_x/Ti_4O_7-300, the crystalline manganese oxide catalyst from our previous work. As shown in Fig. 4A, the ORR halfwave potential and ORR-limiting diffusion current of MnO_x/Ti_4O_7-PMOD were 0.75 V *VS* RHE and -5.21 mA cm^{-2}, respectively, better than those of MnO_x/Ti_4O_7-300 at 0.72 V *vs.* RHE and -4.34 mA cm^{-2}, respectively. As shown in Fig. 4B, the OER performance of MnO_x/Ti_4O_7-PMOD was also better than that of MnO_x/Ti_4O_7-300, with a potential of 1.60 V *vs.* RHE at 1 mA cm^{-2} and an overpotential of 530 mV at 10 mA cm^{-2}; for comparison, MnO_x/Ti_4O_7-300 had a potential of 1.71 V *vs.* RHE and could not reach 10 mA cm^{-2}. Amorphous materials exhibit better ORR/OER performance because they show a high defect state with more abundant edge active sites and more surface-exposed catalytic active sites. A comparison of the ORR/OER performance of the MnO_x/Ti_4O_7-PMOD synthesised in this work and those from other studies is presented in Table S2.† MnO_x/Ti_4O_7-PMOD showed ORR/OER bifunctional catalytic performance, which led us to assemble a lithium–oxygen battery with it for further comparison with the crystalline catalyst MnO_x/Ti_4O_7-300.

The K–L equation and RRDE curves could also be used to further confirm the catalytic performance based on the electron transfer numbers, as shown in Fig. S11–S14.† The electron transfer numbers of MnO_x/Ti_4O_7-PMOD and MnO_x/Ti_4O_7-300, calculated from the K–L equation, were 3.89 and 3.87, respectively. The electron transfer numbers of MnO_x/Ti_4O_7-PMOD calculated from the RRDE curves were 3.86, 3.89, and 3.86 at 400, 900, and 1600 rpm, respectively. The average electron transfer number of MnO_x/Ti_4O_7-PMOD, calculated from the RRDE curves, was 3.87, which is consistent with the K–L result. In contrast, the RRDE-calculated electron transfer numbers of MnO_x/Ti_4O_7-300 were 3.39, 3.39, and 3.42 at 400, 900, and 1600 rpm, respectively. The average electron transfer number of MnO_x/Ti_4O_7-300 from the RRDE curves was 3.40. The electron

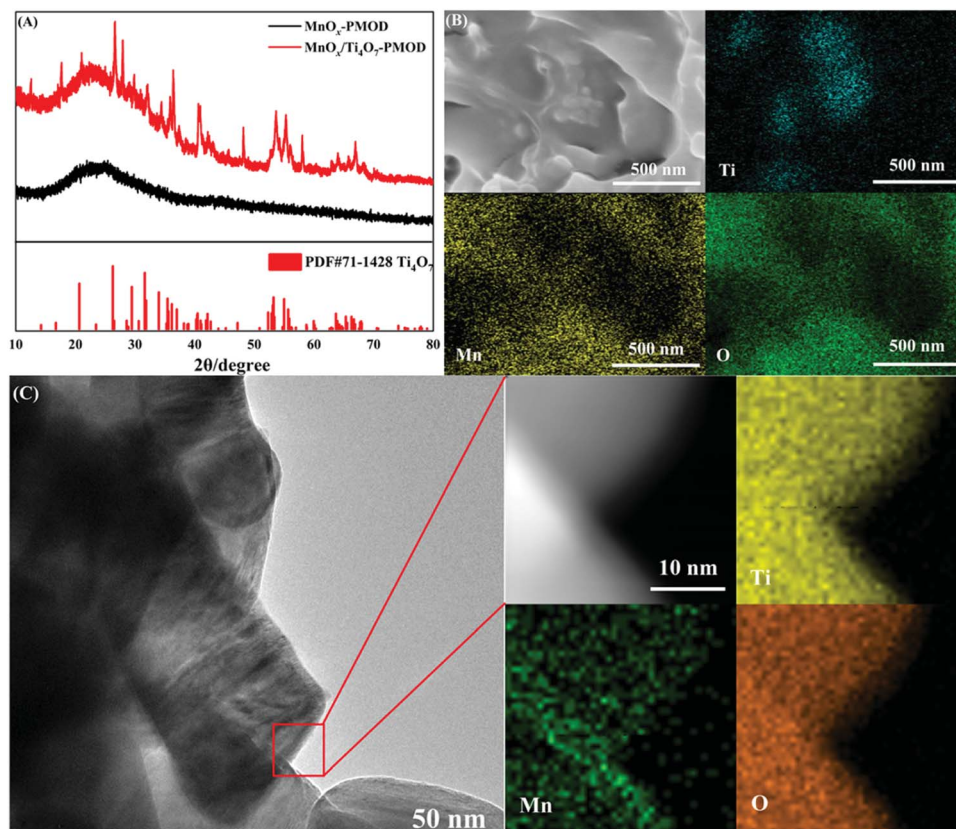**Fig. 3** (A) XRD of amorphous catalysts MnO_x/Ti_4O_7-PMOD and MnO_x-PMOD, (B) SEM of MnO_x/Ti_4O_7-PMOD and corresponding EDS mapping element distribution of Ti, Mn and O, (C) TEM of MnO_x/Ti_4O_7-PMOD and corresponding EDS mapping element distribution of Ti, Mn and O.
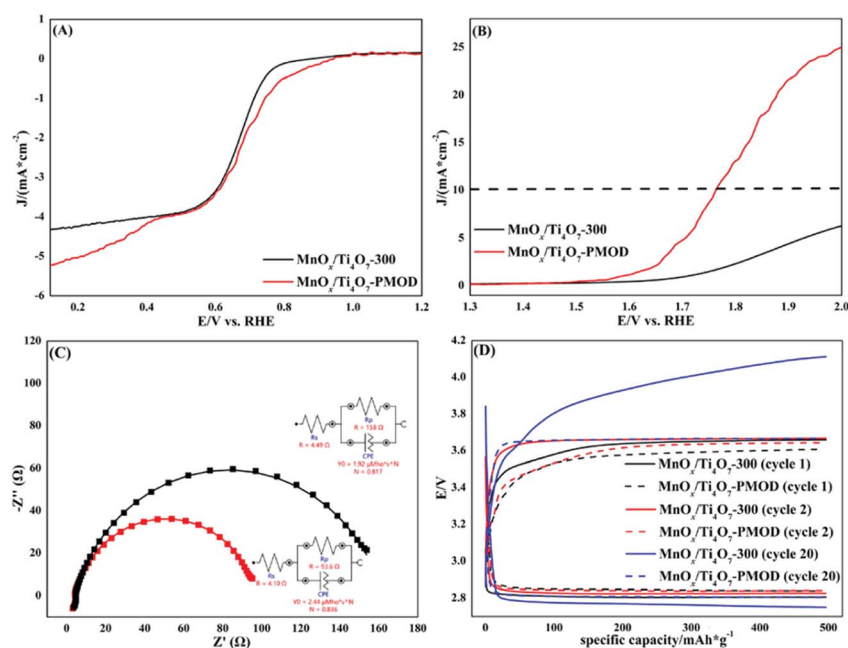

Fig. 4 Comparison of crystalline catalyst MnO_x/Ti_4O_7-300 (black) and amorphous catalyst MnO_x/Ti_4O_7-PMOD (red): (A) ORR, (B) OER, (C) EIS tests and corresponding equivalent circuit of $Li-O_2$ battery, and (D) constant current and capacity performance of $Li-O_2$ battery.

transfer number of MnO_x/Ti_4O_7-PMOD is closer to the theoretical value of 4 than MnO_x/Ti_4O_7-300. This means that MnO_x/Ti_4O_7-PMOD has more efficient O_2 utilisation. The production rate of H_2O_2 (%H_2O_2), calculated from the RRDE curves, also confirms this. The average %H_2O_2 of MnO_x/Ti_4O_7-PMOD was 7.09% compared to 29.90% for MnO_x/Ti_4O_7-300. More oxygen is directly reduced to OH^- than to OH^{2-}.

According to the battery performance comparison shown in Fig. 4C and D, the lithium–oxygen battery assembled with the amorphous catalyst MnO_x/Ti_4O_7-PMOD is better than that assembled with the crystalline catalyst MnO_x/Ti_4O_7-300, which is consistent with the ORR/OER performance results. As shown by the EIS tests in Fig. 4C, the charge transfer resistance of MnO_x/Ti_4O_7-PMOD was 93.6 Ω, smaller than that of MnO_x/Ti_4O_7-300 at 158 Ω. In the constant-current and capacity-performance tests, shown in Fig. 4D, the initial charge–discharge voltage platforms of the two batteries were similar. After 20 cycles, the discharge voltage, charging voltage, and platform voltage difference of MnO_x/Ti_4O_7-PMOD were 2.81, 3.67, and 0.86 V, respectively, while the corresponding values of MnO_x/Ti_4O_7-300 were 2.78, 4.10, and 1.32 V, respectively. After a long period of operation, the polarisation of the MnO_x/Ti_4O_7-300 battery was more obvious than that of the MnO_x/Ti_4O_7-PMOD battery, and the degradation of battery performance was more severe.

A comparison of the MnO_x/Ti_4O_7-PMOD and MnO_x/Ti_4O_7-300 catalysts is shown in Table S3.† Overall, the ORR/OER bifunctional catalytic activity of the amorphous catalyst MnO_x/Ti_4O_7-PMOD was better than that of the crystalline catalyst MnO_x/Ti_4O_7-300, especially in terms of OER catalysis performance. The performance of the lithium–oxygen battery assembled with MnO_x/Ti_4O_7-PMOD was superior to that of the battery assembled with MnO_x/Ti_4O_7-300. The amorphous catalyst prepared in this study not only has excellent ORR/OER bifunctional catalytic performance but also has good prospects for further development and potential for application in metal–air batteries.

4. Conclusions

Amorphous materials exhibit a high defect state with more abundant edge active sites and more surface-exposed catalytic active sites, which improves the catalytic performance. Amorphous materials also tend to form crystals, thereby losing active sites and reducing the catalytic activity. By adding a carrier like Ti_4O_7, the durability and conductivity of amorphous materials can be effectively increased. In this work, we prepared amorphous manganese oxide catalysts that show comparable ORR/OER catalytic performance to catalysts from other studies. Several conclusions can be drawn from this study.

(1) Amorphous manganese oxides were prepared by PMOD and their composition, phase and morphology were proved using SEM, XPS, TEM, Raman spectroscopy, and FTIR spectroscopy. The ratio of Mn^{3+} was different with different UV light irradiation times, which is a key point in the performance of the amorphous manganese oxide catalyst. Among the catalysts prepared with different irradiation times, MnO_x-PMOD48 with

48 h irradiation had the highest Mn^{3+} ratio and showed the best ORR/OER performance.

(2) MnO_x-PMOD48 also showed better ORR/OER performance than the crystalline manganese oxide catalyst obtained in a previous work because of the high defect state with more abundant edge active sites and more surface-exposed catalytic active sites.

(3) Following our previous experience with the use of Ti_4O_7 as a catalyst support for crystalline manganese oxide, we added Ti_4O_7 during the synthesis of MnO_x-PMOD48 and obtained amorphous manganese oxides supported with Ti_4O_7, denoted as MnO_x/Ti_4O_7-PMOD. Ti_4O_7 particles induced the formation of manganese oxides on themselves and supported the catalyst, leading to better stability. Comparing the amorphous catalyst MnO_x/Ti_4O_7-PMOD and crystalline catalyst MnO_x/Ti_4O_7-300, both of which are supported by Ti_4O_7, we can conclude that the amorphous catalyst has better ORR/OER performance.

In the future, we may perform more work to further stabilise the amorphous catalyst for applications like batteries. The PMOD method can also be used for the synthesis of other amorphous materials. This will help us to understand nanoparticles and find more choices for the wider application of metal-air batteries.

Conflicts of interest

There are no conflicts to declare.

Acknowledgements

References

1 M. F. Sanad, A. E. Shalan, S. O. Abdellatif, E. S. A. Serea, M. S. Adly and M. A. Ahsan, *Top. Curr. Chem.*, 2020, **378**, 1–43.

2 K. Kannan, D. Radhika, K. K. Sadasivuni, K. R. Reddy and A. V. Raghu, *Adv. Colloid Interface Sci.*, 2020, **281**, 102178.

3 K. Kannan, D. Radhika, K. R. Reddy, A. V Raghu, K. K. Sadasivuni, G. Palani and K. Gurushankar, *Nano Express*, 2021, **2**, 010014.

4 D. P. Suhas, A. V. Raghu, H. M. Jeong and T. M. Aminabhavi, *RSC Adv.*, 2013, **3**, 17120–17130.

5 D. P. Suhas, T. M. Aminabhavi, H. M. Jeong and A. V. Raghu, *RSC Adv.*, 2015, **5**, 100984–100995.

6 F. Y. Cheng and J. Chen, *Chem. Soc. Rev.*, 2012, **41**, 2172–2192.

7 Y. T. Sun, X. R. Liu, Y. M. Jiang, J. Li, J. Ding, W. B. Hu and C. Zhong, *J. Mater. Chem. A*, 2019, **7**, 18183–18208.

8 D. Banham, S. Ye, K. Pei, J. Ozaki, T. Kishimoto and Y. Imashiro, *J. Power Sources*, 2015, **285**, 334–348.

9 X. M. Ge, A. Sumboja, D. Wuu, T. An, B. Li, F. W. T. Goh, T. S. A. Hor, Y. Zong and Z. L. Liu, *ACS Catal.*, 2015, **5**, 4643–4667.

10 Y. H. Bing, H. S. Liu, L. Zhang, D. Ghosh and J. J. Zhang, *Chem. Soc. Rev.*, 2010, **39**, 2184–2202.

11 N. Tian, Z. Y. Zhou, S. G. Sun, Y. Ding and Z. L. Wang, *Science*, 2007, **316**, 732–735.

12 Y. Lee, J. Suntivich, K. J. May, E. E. Perry and Y. Shao-Horn, *J. Phys. Chem. Lett.*, 2012, **3**, 399–404.

13 K. A. Stoerzinger, L. Qiao, M. D. Biegalski and Y. Shao-Horn, *J. Phys. Chem. Lett.*, 2014, **5**, 1636–1641.

14 M. Sevim, T. Sener and O. Metin, *Int. J. Hydrogen Energy*, 2015, **40**, 10876–10882.

15 K. Kannan, D. Radhika, A. S. Nesaraj, K. K. Sadasivuni, K. R. Reddy, D. Kasai and A. V. Raghu, *Mater. Sci. Energy Technol.*, 2020, **3**, 853–861.

16 W. Xia, A. Mahmood, Z. B. Liang, R. Q. Zou and S. J. Guo, *Angew. Chem., Int. Ed.*, 2016, **55**, 2650–2676.

17 M. Srinivas, C. V. Reddy, K. R. Reddy, P. S. Nagaraj, M. S. Reddy and A. V. Raghu, *Mater. Res. Express*, 2019, **6**, 125502.

18 M. I. A. A. Maksoud, R. A. Fahim, A. E. Shalan, M. A. Elkodous, S. O. Olojede, A. I. Osman, C. Farrell, A. H. Al-Muhtaseb, A. S. Awed, A. H. Ashour and D. W. Rooney, *Environ. Chem. Lett.*, 2021, **19**, 375–439.

19 K. Zhang, X. P. Han, Z. Hu, X. L. Zhang, Z. L. Tao and J. Chen, *Chem. Soc. Rev.*, 2015, **44**, 699–728.

20 J. E. Post, *Proc. Natl. Acad. Sci. U. S. A.*, 1999, **96**, 3447–3454.

21 M. Pourbaix, *Atlas of electrochemical equilibria in aqueous solutions pergamon press*, Pergamon Press, New York, 1966.

22 Y. J. Xue, S. S. Sun, Q. Wang, Z. H. Dong and Z. P. Liu, *J. Mater. Chem. A*, 2018, **6**, 10595–10626.

23 J. Suntivich, H. A. Gasteiger, N. Yabuuchi, H. Nakanishi, J. B. Goodenough and Y. Shao-Horn, *Nat. Chem.*, 2011, **3**, 546–550.

24 J. Rossmeisl, Z. W. Qu, H. Zhu, G. J. Kroes and J. K. Norskov, *J. Electroanal. Chem.*, 2007, **607**, 83–89.

25 J. Suntivich, K. J. May, H. A. Gasteiger, J. B. Goodenough and Y. Shao-Horn, *Science*, 2011, **334**, 1383–1385.

26 J. L. Hodala, D. J. Moon, K. R. Reddy, C. V. Reddy, T. N. Kumar, M. I. Ahamed and A. V. Raghu, *Int. J. Hydrogen Energy*, 2021, **46**, 3289–3301.

27 F. Bai, L. C. Xu, D. D. Wang, L. An, Z. Z. Hao and F. Li, *RSC Adv.*, 2021, **11**, 1524–1530.

28 C. T. Campbell and C. H. F. Peden, *Science*, 2005, **309**, 713–714.

29 H. B. Huang, S. H. Luo, C. L. Liu, Q. Wang, Z. Y. Wang, Y. H. Zhang, A. M. Hao, Y. G. Liu, J. Z. Li, Y. C. Zhai and Y. N. Dai, *J. Alloys Compd.*, 2017, **726**, 939–946.

30 R. Shwetharani, H. R. Chandan, M. Sakar, G. R. Balakrishna, K. R. Reddy and A. V. Raghu, *Int. J. Hydrogen Energy*, 2020, **45**, 18289–18309.

31 A. A. Avey and R. H. Hill, *J. Am. Chem. Soc.*, 1996, **118**, 237–238.

32 H. J. Zhu and R. H. Hill, *J. Non-Cryst. Solids*, 2002, **311**, 174–184.

33 L. S. Andronic and R. H. Hill, *J. Photochem. Photobiol., A*, 2002, **152**, 259–265.

34 S. Trudel, E. D. Crozier, R. A. Gordon, P. S. Budnik and R. H. Hill, *J. Solid State Chem.*, 2011, **184**, 1025–1035.

35 R. D. L. Smith, M. S. Prevot, R. D. Fagan, S. Trudel and C. P. Berlinguette, *J. Am. Chem. Soc.*, 2013, **135**, 11580–11586.

36 R. D. L. Smith, M. S. Prevot, R. D. Fagan, Z. P. Zhang, P. A. Sedach, M. K. J. Siu, S. Trudel and C. P. Berlinguette, *Science*, 2013, **340**, 60–63.

37 C. J. Zhang, S. Trudel and C. P. Berlinguette, *Eur. J. Inorg. Chem.*, 2014, **2014**, 660–664.

38 K. R. Reddy, B. Hemavathi, G. R. Balakrishna, A. V. Raghu, S. Naveen and M. V. Shankar, *Polymer Composites with Functionalized Nanoparticles*, 2019, pp. 357–379.

39 M. F. Sanad, A. E. Shalan, M. A. Ahmeda and M. F. A. Messih, *RSC Adv.*, 2021, **11**, 22352–22364.

40 H. Zhu, F. L. Lyu, M. L. Du, M. Zhang, Q. F. Wane, J. M. Yao and B. C. Guo, *ACS Appl. Mater. Interfaces*, 2014, **6**, 22126–22137.

41 L. M. Wang, W. L. Chen, D. D. Zhang, Y. P. Du, R. Amal, S. Z. Qiao, J. W. Bf and Z. Y. Yin, *Chem. Soc. Rev.*, 2019, **48**, 5310–5349.

42 M. P. Browne, Z. Sofer and M. Pumera, *Energy Environ. Sci.*, 2019, **12**, 41–58.

43 K. M. Zhao, W. W. Zhu, S. Q. Liu, X. L. Wei, G. Y. Ye, Y. K. Su and Z. He, *Nanoscale Adv.*, 2020, **2**, 536–562.